The effects of microstructure and confinement on the compressive fragmentation of an advanced ceramic

James David Hogan[a], Lukasz Farbaniec[a], Matt Shaeffer[a], KT Ramesh[a,b]

[a] *Hopkins Extreme Materials Institute, The Johns Hopkins University, Baltimore, MD 21218, USA*
[b] *Department of Mechanical Engineering, The Johns Hopkins University, Baltimore, MD 21218, USA*

Abstract

We investigate the rate-dependent compressive failure and fragmentation of a hot-pressed boron carbide, under both uniaxial and confined biaxial compression, using quantitative fragment analysis coupled with quantitative microstructural analysis. Two distinct fragmentation regimes are observed, one of which appears to be more sensitive to the microstructural length scales in the material, while the second is more sensitive to the structural character and boundary conditions of the compressed sample. The first regime, which we refer to as "microstructure-dependent," appears to be associated with smaller fragments arising from the coalescence of fractures initiating from graphitic inclusions. This regime appears to become more dominant as the strain rate is increased and as the stress-state becomes more confined. The second regime generates larger fragments with the resulting fragment size distribution dependent on the specific structural mechanisms that are activated during macroscopic failure (e.g., buckling of local columns developed during the compression). The average fragment size in the latter regime appears to be reasonably predicted by current fragmentation models. This improved understanding of the effects of microstructure and confinement on fragmentation then provides new insights into prior ballistic studies involving boron carbide.

Email address: `jd.hogan@jhu.edu` (James David Hogan)

Keywords: dynamic fragmentation, boron carbide, brittle failure, experimental mechanics

1. Introduction

The design of the next generation of light-weight and high-strength advanced ceramics (e.g., hot-pressed silicon carbide [1, 2], aluminum nitride [3], titanium diboride [4]) used in shielding applications requires an improved understanding of their unique dynamic behaviors. In particular, additional insight is needed on the failure and fragmentation mechanisms that exist for high-rate loading conditions under well-defined stress-states (e.g., compression, confinement). Further, connecting these failure mechanisms to the microstructural features will provide insight into the factors that control ceramic performance. In this paper, we investigate the link between the microstructure and the failure and fragmentation of hot-pressed boron carbide in uniaxial and biaxial confined compression.

Failure mechanisms generally are stress-state and strain-rate dependent [3], and an understanding of such mechanisms can provide insight into the design of new and improved ceramic systems. For example, Chen et al. [5] used the appearance of nanoscale intragranular amorphization in ballistic studies to explain the observed decrease in the apparent strength of boron carbide beyond a critical impact velocity. Both experiments and models have shown that the defect distributions have strong effects on the dynamic failure of brittle materials (e.g., [6–8]). Early ballistic studies by Wilkins et al. [9] noted changes in ballistic performance for changes in ceramic microstructures. Swab et al. [10] observed changes in damage and fracture behavior with varying microstructure in silicon carbide. A separate study by Bakas et al. [2] on a hot-pressed silicon carbide linked carbonaceous defects to failure during ballistic loading.

In this paper, we seek to understand the link between carbonaceous defects and the dynamic failure and fragmentation processes in a hot-pressed boron carbide. The fragmentation of ceramics is an effective process for dissipating impact energy in ceramic armor applications. Moreover, fragmentation may lead to erosion of the projectile [11, 12], and resistance to comminution has been identified as an important factor affecting ballistic performance [13].

Much of our understanding of the dynamic fragmentation of brittle materials has been centred around predicting average fragment sizes and the associated distribution of sizes. The bulk of this work has been done for tensile stress-states. Mott [14, 15] pioneered early studies on fragmentation. He considered the origin of fracture sites within an idealized cylinder and the propagation of tensile release waves away from these fracture sites. Mott's [14, 15] work is summarized in the book by Grady [16]. In Grady's [17] energy-based fragmentation theory, the kinetic energy of expansion is compared with the energy required to create new fragment surfaces. Grady's analytical model predicts that the average fragment size would decrease with increasing strain rate to the power of 2/3. Experimental results of fragmentation of brittle materials have shown this model over-estimates the average fragment size by orders of magnitude at intermediate strain rates [18]. Glenn and Chudnovsky [19] extended the work of Grady [17] to include the elastic strain energy contribution, which is important at low strain-rates. They predicted a quasi-static average fragment size that is independent of strain rate for low and intermediate strain rates, but does coincide with Grady's 2/3 power at high rates. More recently, Zhou et al. [20, 21] (ZMR) and Levy and Molinari [22] (LM) developed average fragment size predictions by simulating the fragmentation of expanding brittle rings. In their models, the evolution of the residual damage was accounted for, as well as the wave reflections and interactions that may either suppress or activate crack growth. Experimental fragmentation results derived from impacts on rock have shown to be reasonably well described by the ZMR and LM predictions [18, 23]. However, we note that limited experimental measurements exist, especially at very high rates.

In this paper, we explore the relationships between processing-induced defects and the fragmentation of boron carbide during uniaxial unconfined and bi-axial confined compression. Methods are introduced to quantify flaw and fragment size distributions, and dominant flaw types are identified. Our measurements allow us to link the mesoscale failure mechanisms, the defect distributions, and the fragmentation distributions. The understanding gained from linking the microstructure and fragmentation are used to provide insights into the ballistic performance of boron carbide from a recent paper by Sano et al. [24].

2. Experimental Methods

Quasi-static and dynamic uniaxial and bi-axial confined compression experiments were performed on a hot-pressed boron carbide from Coorstek (Vista, California), with a Young's modulus of 430 GPa, a density of 2,490 kg/m^3 and Poisson ratio of 0.16. These measurements are provided by the manufacturer and have been confirmed by us. Cuboidal specimens were used (5.3 mm in length, 3.5 mm in width and 4.0 mm in height). Quasi-static experiments were performed using an MTS servo-hydraulic test machine with a controlled displacement rate at a nominal strain rate of 10^{-3} s^{-1}. The dynamic compression experiments were performed using a Kolsky bar apparatus for rates between 200 and 500 s^{-1}. This is the same Kolsky bar setup as Kimberley et al. [25] and a schematic is shown in Figure 1. The Kolsky bar setup consists of a striker projectile, and incident and transmitted bars, each made of C-350 maraging steel with a density of 8,100 kg/m^3 and Young's modulus of 200 GPa. The bars had a common diameter of 12.7 mm, and the incident and transmission bars were 1,220 and 1,060 mm in length, respectively. In a Kolsky bar experiment, the striker projectile impacts the incident bar and an elastic wave (stress pulse) is generated (left in Figure 1). Pulse shappers may be placed between the bar and the projectile in order to obtain a specific shape of the stress pulse. In our experiment, an annealed copper and graphite pulse shapers were used to impose a triangular loading pulse on the sample. After the pulse is shapped, it propagates down the incident bar and the magnitude of its strain (ϵ_i) is recorded over time by strain gauge 1. Here, the subsript i denote indicident. The wave then passes through the sample, and this loads the sample until failure ("sample" labeled in Figure 1, with an inset image highlighted in the red rectangle). A set of impedance-matched platens were placed between the sample and end faces of the input and output bars to prevent sample indentation. Each platen (diameter: 12.7 mm, thickness: 5.0 mm) consisted of a tungsten carbide disk that had been confined by a heat-shrunk Ti6Al4V collar. High-vacuum grease was applied on the curved contacting surfaces to minimize friction. After passing through the sample, the magnitude of pulse is recorded by strain gauge 3 (ϵ_T), while some of the wave is reflected from the sample and measured by strain gauge 2 (ϵ_R). Here the subsripts T transmitted, and R refeclected. The stress in the sample is then calculated as:

$$\sigma = \frac{A_b}{A_s} E_b \epsilon_T \tag{1}$$

where A_b and A_s is the cross-sectional area of the bar and specimen, respectively, and E_b is the Young's modulus of the bar.

In addition to uniaxial compression, experiments are also performed in bi-axial compression. An inset of the bi-axial confinement schematic is also shown Figure 1 (right).

Rigid confinement is applied vertically, the material is loaded horizontally, and the material is allowed to expand in the other direction. Additional details about the experimental design for the bi-axial confinement apparatus is described in Paliwal et al [6]. In the present experiments, the static confining pressures used were 300 MPa and 500 MPa. A Kirana Ultra High-Speed Camera operating at 2 Mfps with a 500 ns exposure time captured time-resolved failure and fragmentation processes for the uniaxial dynamic compression experiments. A Shimadzu high-speed camera operating at 5 Mfps with a 100 ns exposure time captured sample failure during bi-axial confinement experiments. Output pulses from the cameras were used to synchronize the camera images with the stress-time history recorded by the strain gauge on the transmitted bar. Camera and strain gage pulses are recorded using the same data acquisition system. Synchronization is done by time-shifting the transmitted strain gage pulse to the sample location by knowing the distance between the sample and the strain gage, and the speed of sound in the bar. The strain gage signal and individual output pulses for each camera frame are then synched. Following the experiments, a Zeiss optical microscope with an AxioCam MRC camera was used to image the fragments, and features inside of the fragments (once they were mounted in resin and systematically polished).

3. Experimental Results

In this section, we describe the observed characteristic features in the microstructure and the fragmentation of boron carbide. The different types of microstructural features (e.g., flaws and inclusions) are introduced, the key types of defects governing failure are identified, and methods for quantifying statistics (e.g., spacing) are presented. Mesoscale (> grain size) failure mechanisms developed under uniaxial and biaxial compression are then examined. Lastly, the measured fragmentation distributions are presented and compared to characteristic length scales of the microstructural features.

3.1. Microstructure of Hot-Pressed Boron Carbide

The major microstructural features in the hot-pressed boron carbide material are shown in the optical microscope image in Figure 2a. The hot-pressing direction is vertical in this image. Elongated inclusions are observed which are graphitic in composition, confirmed with Energy Dispersive Spectroscopy (EDS) measurements. Examination of other sections shows that these elongated graphite particles are in-fact disk-like in three-dimensions. Also highlighted in Figure 2a are smaller and more circular features. These are primarily comprised of smaller graphitic inclusions, with even smaller features consisting of cavities/pores (both confirmed with scanning electron microscopy). Bright phases are also noted in Figure 2a, which are primarily comprised of aluminum nitride (AlN) (confirmed with EDS and transmission electron microscopy). These aluminum nitride inclusions are faceted structures, and are between 1 and 20 μm in size. Additional and rare phases include boron nitride (BN), which are generally too small to be identifiable at this scale (which we define as mesoscale).

Images of the microstructure are converted to grayscale (not shown), which still show the graphite defects as dark features, and the AlN inclusions as bright features. Next, we use image processing tools in Matlab to convert the grayscale optical microscope images to monochrome using thresholding. A sample black and white image after thresholding is shown in Figure 2b. Image processing techniques are applied to the monochrome images to determine feature of the white features, including: particle sizes (by fitting an ellipse to each particle and measuring major and minor axis dimensions), orientation (direction of major axis of the fitted ellipse), and particle centroids. Centroids are used to determine the spacing between adjacent features. We also match the pixel values of the white features to those values in the greyscale image, and this allows us to get an average pixel greyscale color intensity. We associate high greyscale color intensity with the AlN/BN phases, and this allows us to isolate those defect types from the total population. We set a threshold conditions for the aspect ratio of the major and minor axes as 2.5 for distinguishing between the spherical graphitic features and the graphitic disks. Classifying defect types allows the defect density (#/m^2) and spacing (ℓ_n) to be computed. Defect statistics are obtained for a total of 350 distinct images at a magnification of 100x. This image analysis process is schematically shown in Figure 3. In this study, we are particularly interested in the spacing between the graphite disks as this will be linked later with fragment size distributions. Fragment sizes are also computed using similar methods to those shown in Figure 2.

3.2. Failure Mechanisms During Dynamic Loading

A typical stress-time history curve (on the left) with time-resolved high-speed video images (on the right) for the uniaxial dynamic compression experiment is shown in Figure 4. The stress-time plot is generated during a Kolsky bar experiment. The peak stress is 3.90 GPa (i.e., this is called the compressive strength) and the corresponding failure image is shown in t_2. A total of six images (t_1 to t_6) are used to highlight the failure modes (right) and these are selected for 2 μs intervals. The loading direction is horizontal in the video images. The stress rate, $\dot{\sigma}$, is 200 MPa/μs (determined as the slope of stress-time plot between 10 and 90 % of the peak stress). For reference, the linear approximation used to calculate the stress rate is shown as the dashed line. The corresponding strain rate, $\dot{\epsilon}$, is estimated by dividing the stress rate by the Young's modulus. In the example shown in Figure 4, the strain rate is estimated as 465 s^{-1}.

At time t_1 (prior to peak stress), there is a visible axial crack that has propagated fully across the sample. This fracture does not appear to initiate from the corners of the sample and is oriented in the direction of maximum compression [26]. Additional fractures are not visible on this surface at the time (t_2) of the peak stress. After the peak stress is reached, the total damage continues to grow to dissipate the strain energy, while the stress in the material decreases. Edge failure at the top right corner is observed at t_3, although no additional axial cracks are visible. At t_4, 4 μs after peak stress, the damage has propagated from right to left from the initial failure area in the image at t_3. Transverse cracks perpendicular to the compressive loading direction are also observed at t_4. Transverse cracks are believed to occur as a result of the buckling of the columns [27] formed from the spanwise propagation of the axial cracks at earlier times. At later times (t_5 and t_6), additional axial and transverse cracks rapidly develop across the sample, these cracks coalesce, and the stress in the material collapses. The coalescence of axial and transverse cracks appears to result in the generation of fragments that are between 830 and 1,600 μm in size at time t_6. Measurements of velocity of the axial cracks range from approximately 1,800 to 2,400 m/s (ten total measurements across multiple tests) with an average of 2,000 ± 300 m/s.

As a counterpoint, we present the stress-time history and associated time-resolved mesoscale failure modes in the dynamic bi-axial confined compression of boron carbide (Figure 5). In the time resolved images, the confining stress is applied in the vertical direction, along the top and bottom of the cuboidal specimen (confinement platens labeled in t_5). Note that the dynamic loading is again along the horizontal in the images. In this experiment, the confining pressure is 300 MPa, the observed peak stress is 4.20 GPa, and the stress rate is 175 MPa/μs. Prior to peak stress, there are no visible cracks at t_1 despite the stress levels here of 4.0 GPa being larger than the peak stress for the uniaxial compression case in Figure 4. At the time of the peak stress (t_2), we begin to observe cracking (arrows) at the right side of the sample. At time t_3, 2 μs after peak stress, the failure is observed to primarily grow from right to the left, while some of the failure has propagated downward. Prior to peak stress (t_2), there is little fracturing that is visible on the imaged face of the specimen. Post-peak stress, the failure propagates across the sample from right to left. In the bi-axial confined case, initial fractures are observed to propagate perpendicular to dynamic the loading direction (t_4), in contrast to the uniaxial compression case, where the initial cracks are along the loading direction. As damage further develops to the right at t_4, the stress continues to relax (now 3.80 GPa). Now visible at t_4 are multiple cracks that span across the sample in a direction perpendicular to the loading direction, spaced approximately 200 to 500 μm apart. There are more spanning cracks in the bi-axial confined case than in the uniaxial compression case, possibly a result of the additional strain energy in the bi-axial confined case. At later time (t_5 and t_6), the damage continues to propagate to the right at a speed of approximately 510 ± 130 m/s (taken for multiple tests with minimum of 300 m/s and maximum 800 m/s). The columns formed from the spanning perpendicular fractures have buckled and the stress curve continues to collapse. There are many more buckling fractures in bi-axial compression than in the uniaxial compression case. This should lead to smaller observed fragments than in the uniaxial compression case. In the next section, we link the buckling mechanisms to measurements of the fragmentation size distributions.

3.3. Brittle Fragmentation

In this subsection, the resulting boron carbide fragment size distributions are examined. Images of a collection of fragments are taken, converted to grayscale, and then thresholding is used to convert the images to monochrome, where fragments appear as white features in the images. Image processing in Matlab is used to determine their size

(ℓ), projected area (A) and perimeter (P). Shown in Figure 6 are the empirical cumulative distributions of the fragment major axis size derived during quasi-static (strain rate of 10^{-3} s^{-1}) and dynamic (strain rate of 400 s^{-1}) uniaxial and bi-axial compression. The confining pressure for the bi-axial experiments is 500 MPa. Note that some uncertainty exists for fragments <30 μm as these may lost during collection and imaging. If the probability distribution of fragment sizes is $g(\bar{x})$, then the cumulative distribution function is given as:

$$G(x) = \int_0^x g(\bar{x}) d\bar{x} \quad (2)$$

The fragment size data set is a discrete set of n fragments with sizes ℓ_i (i=1...n). Ordering this data in terms of increasing fragment size, and assigning a probability of $1/n$ to each fragment, we compute the empirical cumulative distribution function, or eCDF, as the sum of these probabilities.

$$G_e(\ell) = \frac{1}{n} \sum_{i=1}^{n} I(\ell_i \leq \ell) \quad (3)$$

where the indicator function I has a value of 1 if $\ell_i \leq \ell$ and 0 otherwise. The eCDF approximates the CDF when the number of fragments is large. In our case n>1,500, and so the eCDF is a useful measure.

We begin by discussing the quasi-static uniaxial compression experiment (thin solid blue curvse in Figure 6). Most of the fragments are between 10 μm and 1 mm in size, and the eCDF shows a bump (and an inflection) at just under 100 μm. We believe this suggests that two different fragmentation mechanisms may be present. Since the eCDF represents the relative frequency, we see that about 30 % of the fragments generated by quasi-static uniaxial compression are less than 100 μm in size. The eCDF associated with the fragments generated under dynamic uniaxial compression are shown in Figure 6 using the dashed thin blue curve. The curve is shifted to the left compared to the quasistatic uniaxial compression case (solid thin blue line), demonstrating that the high strain-rate experiment generally produces smaller fragments. Note that the bump at just under 100 μm in size persists, and we see that about 40 % of the fragments generated by dynamic uniaxial compression are less than 100 μm in size. We divide the distributions in Figure 6 by fragment size at a size of 100 μm, with the domain ℓ_i<100 μm called fragmentation Regime I, and that with ℓ_i>100 μm called Regime II. Regime I comprises 30 % of the total population at rate of 10^{-3} s^{-1} and 40 % at a rate of 400 s^{-1}.

When the material is bi-axially confined at 500 MPa (solid and dashed thick red curves in Figure 6), the eCDFs are generally to the left of the corresponding uniaxial compression curves, and, again, the dynamic eCDF is to the left of the quasistatic eCDF. There is also an increase in the total number of fragments < 100 μm in size. We also note here that the failure mode and fragmentation features are similar between the dynamic 300 MPa case shown in the high-speed video images (Figure 5), and the dynamic case confined at 500 MPa shown here. For biaxial confinement, Regime I comprises 55 % of the total population at rate of 10^{-3} s^{-1} and 64 % at a rate of 400 s^{-1}.

Why are there two regimes in the fragmentation curves? To understand this, we also present the eCDF of the graphitic disk spacing as the green curve in Figure 6. Very nearly all of the disks are less than 100 μm apart, suggesting that Regime I fragments may be related to the spacings between adjacent graphitic disks. Further evidence of the importance of the graphite disks in fragmentation processes is shown in Figure 7. Fracture initiation and propagation behaviors inside of fragments are examined in the optical microscope image in Figure 7. This fragment was generated during a dynamic uniaxial compression experiment at a strain rate of 400 s^{-1}. Fragments were collected following experiments, mounted in resin, and systematically polished to a sub-micron finish to allow internal features to be examined. Elongated graphitic particles are observed to be intersecting the curved fracture surface. These particles are in-fact disk-like in three-dimensions and we believe that fracture is initiated from these defects. Fractures initiated from the disks are believed to coalesce with fractures from other disks, and for this reason, there is an inherent relationship between the disk spacing and Regime I fragment sizes. Image from the bi-axial experiments show similar evidence.

The connection between disk spacing and fragment sizes is best seen by comparing the defect spacing and fragment distributions in a quantile-quantile plot as shown in Figure 8. A quantile-quantile (QQ) plot is a graphical method for comparing two distributions. Quantiles of the two distributions are plotted against each other; if the distributions are similar, the points will lie on a line. Quantiles are points taken at regular intervals from the cumulative distribution function of a random variable. Consider two ordered sets of data (in this case, disk spacing data and fragment size data):

$$x_{(1)}, x_{(2)}, ...x_{(m)} \tag{4}$$

and

$$y_{(1)}, y_{(2)}, ...y_{(n)} \tag{5}$$

where $m \leq n$, and with probability distribution functions of $g(x)$ and $f(y)$. The corresponding cumulative distribution functions (CDF) are $G(x)$ and $F(y)$. Quantiles divide the ordered sets in terms of the CDF into equal subsets. For example, the 2-quantile (q_2) is called the median and it divides the set into 2 equal parts. The corresponding median values occurs when $G(x)$ or $F(y)$=1/2. The 4-quantiles (q_4) are called quartiles and q_4 divides the ordered population into 4 equal parts. The 100-quantile (q_{100}) are called percentiles. Generally, there exists an x or y such that $G(x)$ or $F(y)=\mathrm{q}_n$. This allows us to compare x and y values in their respective units. For example, in Figure 8 the actual quantile level is not plotted, instead both axes are measured in their respective data sets. However, for a given (x,y) on the q-q plot, the quantile level is the same for both points. If the data sets have the same size, the q-q plot is essentially a plot of sorted data set 1 against sorted data set 2. If the data sets are not of equal size, which is the case here, the quantiles are selected to correspond to the sorted values from the smaller data set and then the quantiles for the larger data set are interpolated (linearly in this case). Lastly, to help the visualization, we include a red dashed reference line Figure 8 between the first and third quartiles and extend the curve to cover the range of data. In Figure 8, we only consider the subset of fragment sizes < 100 μm. The agreement between the fragment size data (blue line) and the graphite disk spacing (red line) suggests that the two distributions are similar up to 70 μm, indicating a relationship between defect spacing and fragment size in Regime I.

Additional insight into the two fragmentation regimes is obtained by plotting the fragment circularity against the major axis size in Figure 9a for dynamic uniaxial compression and Figure 9b for dynamic bi-axial compression. The circularity, Φ, is defined as:

$$\Phi = \frac{r1}{r2} = \frac{\sqrt{A/\pi}}{P/2\pi} = \frac{2\sqrt{\pi A}}{P} \tag{6}$$

where $r1$ is the equivalent radius of a fragment determined from a fragment projected area (A), and $r2$ is the equivalent radius of a fragment determined from its perimeter (P). For the case of a circle, the circularity is equal to 1. For the case of a rectangle, the circularity is equal to:

$$\Phi_{rect} = \frac{\sqrt{\pi\alpha}}{1+\alpha} \tag{7}$$

where α is the aspect ratio of the rectangle. We note that the data with Φ>1 typically arises from pixelation errors in the optical imaging process for small fragments. Consider first the uniaxial compression case (Figure 9a). The two fragmentation regimes can be more clearly defined in this figure, where the clumping is apparent.Regime I has a circularity between approximately 0.6 and 1.2 and fragment sizes <70 μm. This regime is believed to be associated with the coalescence of fracture initiated from the graphite disk particles for the reasons articulated earlier. We refer to this fragmentation mechanism as microstructure-controlled. Regime II has a circularity between 0.6 and 0.9 and fragments size >100 μm. Fragmentation Regime II is believed to be comprised of larger fragments formed from the buckling mechanism described by Ashby and Hallam [27]. The fragments measured appear to be of similar size as those larger fragments observed in Figures 4 and 5 that formed from the intersection of axial and transverse cracks (i.e., structural failure process). We hypothesize that this fragmentation mechanism is structure-controlled, in that their sizes are determined by which macroscopic failure modes are available, which in turn is related to structural geometry and boundary conditions. Additional consideration is given to structural fragmentation in the discussion that follows. Finally, the dynamic bi-axially confined experiment at a strain rate of 400 s^{-1} is shown in Figure 9b. Here, 64 % of fragments are contained in the microstructure-dependent Regime I.

4. Discussion

In this section, the quantification of the microstructural defect features and the fragmentation results are coupled with our current understanding of the compressive failure of brittle materials. We use this improved understanding to provide new insights into the ballistic response of boron carbide.

4.1. Compressive Brittle Failure

The wing-crack mechanism is typically used to describe the compressive failure of brittle materials [26]. In this mechanism, tension cracks are nucleated at the tip of individual inclined flaws (modelled as slit flaws) and grow to maximize the mode I stress intensity factor [28].

As the compressive loading proceeds, cracks will continue to grow until a critical rate of damage is achieved [29]. At this point the peak stress (i.e., compressive strength) is reached, the material begins to lose its load-carrying capacity, and massive failure ensues. During failure, the damage rate increases rapidly as more cracks are nucleated, crack coalescence occurs, the stress curve collapses and structuralization follows (i.e., the onset of fragmentation).

This study focuses on mesoscale structural failure mechanisms in dynamic uniaxial and bi-axial dynamic compression. In the uniaxial compression case, surface-breaking axial cracks growing along the direction of maximum compression (i.e., in the loading direction) were observed prior to the development of the peak stress. Additional fractures were not visible on the surface at peak stress. It has been suggested that it is the rate of damage growth that determines the peak stress [29], rather than the spanwise propagation of a single axial crack and this is consistent with our observations. The axial crack velocities in this boron carbide material are observed to be, on average, 2,000 ± 300 m/s, which is 23 % of the shear wave speed (estimated as $\sqrt{E/2(1+\nu)\rho}$= 8.4 km/s. The axial splitting mode of compressive brittle failure is well-known [12, 26, 30, 31]. At later times, the columnar structures formed by the axial cracks fail by buckling, causing transverse cracking (e.g., time t_4 in Figure 4). Consequently, the stress in the material collapses. The coalescence of transverse and axial cracks is believed to form the larger fragments.

In the bi-axial cases, there are no visible surface cracks prior to the peak stress despite having stress levels in the material greater than the uniaxial compression peak strength. The ability of the material to absorb additional stress prior to failure is generally believed to primarily be a result of the confinement, although the variability of the microstructure between samples may also contribute to the observed increase in strength. In this particular case, no surface cracks are observed at peak stress in bi-axial compression. As failure proceeds, fractures become visible and these grow perpendicular to the dynamic loading direction (also perpendicular to the axial crack growth in the uniaxial compression case), damage proceeds across the sample, and the stress pulse collapses. There are more "buckling" fractures than in the uniaxial compression case and this leads to smaller fragments.

4.2. Fragmentation

In this boron carbide material, two distinct fragmentation mechanisms were observed in Figure 6 as a result of compressive failure:

1. Regime I. circularity between 0.6 and 1.2 and fragment sizes $<70\,\mu$m. This region appears to be "microstructure-dependent" (Figure 9b).
2. Regime II. circularity between 0.6 and 0.9 and fragment sizes $>100\,\mu$m. This region is believed to be "structure-dependent" as outlined in the subsequent subsections.

Minimal fragmentation was observed between 70 and 100 μm. We attribute the differences in circularity to pixelation of smaller fragments and, therefore, do not focus additional attention on discussing fragment circularity differences. Instead, we explore both regimes by considering the distinct differences in their sizes.

4.2.1. "Microstructure-Dependent" Fragmentation

Regime I fragmentation appears to correlate with the spacing between adjacent graphitic disks (Figure 8). In this fragmentation mechanism, we hypothesize that fractures that are initiated from the graphitic disks through the wing-crack mechanism coalesce with each other to form these smaller fragments. This fragmentation mechanism becomes more important (as shown in Figure 6) as the strain rate is increased and the stress-state becomes increasingly confined, representing 64 % of the total fragment population for the bi-axially confined case at a rate of 400 s^{-1}. Previous investigations [6–8] have suggested that increasing the rates of loading can interrogate increasingly smaller length scales in a brittle ceramic. It is possible, therefore, that other features in the microstructure may activated and dominate behavior under more extreme conditions than those studied here. Stated more generally: each material has a range of inherent length scales, and as we change the strain rate or stress state, the failure and fragmentation mechanisms may explore these length scales.

4.2.2. "Structure-Dependent" Fragmentation

In this section, we investigate Regime II, which we associated with "structure-controlled" fragmentation. Regime II fragments are believed to be formed by the coalescence of the axial and transverse cracks (Figures 4 and 5). In what follows, we develop a theoretical framework for predicting average fragment sizes in Regime II by modelling the buckling of the columnar structures via axial splitting through an expanding ring approximation. The numerical simulation of expanding brittle rings has been previously used by Zhou et al. [20, 21] to model tensile fragmentation and predict rate-dependent average fragment sizes. Analytical expressions have also been developed for average fragment sizes derived for tensile loading by Grady [32]. In this section, we compare the average fragment size from Regime II with theoretical predictions by Grady [32] and Zhou et al. [20, 21].

4.2.3. Theoretical Predictions

The classical model of Grady [32] predicts that the average fragment size would be:

$$L_{Grady} = \left(\frac{48G_c}{\rho\dot{\epsilon}^2}\right)^{1/3} \tag{8}$$

where

$$G_c = \frac{K_{Ic}^2}{2\rho c^2} \tag{9}$$

where G_c is the fracture energery (J/m^2) and K_{Ic} is the fracture toughness (Pa $\sqrt{m}$), ρ is the material density (kg/m^3), c is the elastic wave speed (m/s), and $\dot{\epsilon}$ is the strain rate (s^{-1}). Recent models have attempted to account for wave propagation and material microstructure (e.g., orientation and lengths of flaws, and their spacing), which have been shown to govern the dynamic failure and fragmentation of brittle materials. These include the dynamical fragmentation models developed by Zhou et al. [20, 21], inspired by the earlier works of Drugan [33] and Shenoy and Kim [34]. Zhou et al. [20, 21] (ZMR) incorporated elastic wave propagation and interactions, crack nucleation and growth, and varied material properties into their simulations of expanding rings. The ZMR average fragment size is predicted as:

$$L_{ZMR} = \frac{4.5EG_c}{\sigma_t^2}\left[1 + 0.77\left(\frac{\dot{\epsilon}}{c\sigma_t^3/E^2G_c}\right)^{1/4} + 5.4\left(\frac{\dot{\epsilon}}{c\sigma_t^3/E^2G_c}\right)^{3/4}\right]^{-1} \tag{10}$$

where σ_t is the quasi-static tensile strength of the material (Pa) and E is the Young's modulus (Pa). The characteristic time (t_0), characteristic fragment size (L_0) and characteristic strain rates ($\dot{\epsilon}_0$) introduced by Zhou et al. [21] can be used to normalize the measured and predicted average fragment sizes: $t_0 = \frac{EG_c}{\sigma_t^2 c}$, $L_0 = ct_0$, and $\dot{\epsilon}_0 = \frac{\sigma_t}{Et_0}$. A number of material parameters are needed to apply to these models. Table 1 shows a list of relevant material properties used to compute the characteristic size and strain rate terms. The fracture toughness of boron carbide is obtained from the Coorstek PAD B4C specification sheet. Lacking specific data, the quasi-static tensile strength, σ_t, is assumed to be 1/10 of the measured quasi-static uniaxial compressive strength. The choice of a ratio of 1/10 is motivated by tensile and compressive strengths found in the handbook by Charles [35]. The corresponding values of L_0 and $\dot{\epsilon}_0$ are shown in Table 2. We now consider how these models can be compared to our experimental data, focusing on Regime II, so that the microstructure length scales do not color the problem.

4.2.4. *Comparison of Regime II Fragments with Theoretical Predictions*

Experimental average sizes for structural fragmentation in Regime II are obtained by considering all fragments larger than 100 μm. A comparison of these measured sizes with models requires the definition of an equivalent tensile strain rate ($\dot{\epsilon}_{equi}$), since the models all assume tension. We define the equivalent tensile strain rate by defining an equivalent expanding ring problem with:

$$\dot{\epsilon}_{equi} = \frac{V}{R} \tag{11}$$

where R (m) is the equivalent expanding ring radius and V (m/s) is the velocity of the expansion of the equivalent expanding ring. We can estimate V by assuming that the strain energy in compression is converted to the kinetic energy of an expanding ring.

The strain energy (W) in compression is given as:

$$W = \left[\frac{1}{2}\int \sigma' d\epsilon\right]\nabla = \frac{1}{2}\frac{\sigma t^3}{E} \quad (12)$$

where ϵ is the strain, σ' is the deviotoric stress (Pa), ∇ is the volume (m^3) and t is the specimen size (here we are assuming a cube). The kinetic energy of an equivalent expanding ring is given as:

$$KE_{ring} = \frac{1}{2}mV_{ring}^2 = \frac{1}{2}\rho(2\pi r)RtV_{ring}^2 = \pi\rho R^2 tV_{ring}^2 \quad (13)$$

where m is the mass (kg). Equating these energies (W=KE) and solving for V_{ring}, we find:

$$V_{ring} = \sqrt{\frac{\sigma'^2 t^2}{\pi\rho R^2 E}} \quad (14)$$

and correspondingly

$$\dot{\epsilon}_{equi} = \frac{V_{ring}}{R} = \sqrt{\frac{\sigma'^2 t^2}{\pi\rho R^4 E}} \quad (15)$$

we assume that R is as 10x the specimen length (R=53 mm). The value of R captures the specimen size-dependence of this proposed fragmentation process. Other radii may be assumed (e.g., 30x specimen length), but our results are relatively insensitive to this change because the applied rate is so low (±3% in size prediction difference for 5x to 30x), and that the changing the value of R would only shift the curve horizontally to the left or the right slightly. It is worth noting here that $\dot{\epsilon}_{equi}$ is not equal to the original compressive loading rate. A summary of average fragment size ($\bar{\ell}$), standard deviation, deviotoric stress (σ') and estimated equivalent strain rates ($\dot{\epsilon}_{equi}$) are shown in Table 3.

The corresponding normalized experimental average fragment sizes and strain rates are shown in Figure 10, together with the corresponding average fragment size from the models. The experimental values are reasonably well captured by the ZMR model [21] but are an order of magnitude smaller than the classical model of Grady [32], highlighting the dependence of the larger fragmentation mechanism on energetics and wave interactions associated with structural fragmentation. Note that the choice of R has little impact on the conclusion. We also note the challenges in obtaining statistically significant results over these strain rates, which we believe may suggest two things: 1. the complete fragmentation distribution (i.e., Figure 6) may provide a better metric to compare brittle fragmentation experiments, provided such measurements are complete. 2. additional experimental data is needed at much higher rates in order to test the full application of the current theories. Alternatively to testing material at higher rates, other types of materials can be used to examine regions to the right of the current data set in the normalized size and strain-rate space.

4.3. Comments on Ballistic Performance

We now seek to use our current understanding of the effect of microstructure and confinement on the fragmentation of boron carbide to provide additional insight into the ballistic performance of these materials. We note first that the ballistic performance is a system performance measure, rather than a material performance metric. A commonly used target system for terminal ballistic tests involves a plate, or tile, impacted by a projectile, and here ballistic performance can be quantified in multiple ways:

1. By using a metric (termed v_{50}) based on the velocity at which the tile being impacted stops the projectile 50 % of the time. Beyond this velocity, the probability of defeating the projectile decreases. Below this velocity, the probability of stoping the projectile increases.

2. By measuring the depth of penetration achieved by the projectile for a given velocity.
3. By quantifying, or in most cases qualifying, the post-impact projectile residual velocity and damage.

In a 2014 review of factors affecting ballistic performance, Krell and Strassburger [36] investigated the effects of different microstructures, mechanical properties and the effect of a plate backing in an attempt to order the importance of these factors to ballistic performance. In their study, they defined the "microstructure" in terms of grain size, considering fine and coarse grained polycrystalline ceramics, and single crystals. In our analysis of ballistic performance work we consider different microstructures to be of fixed grain size, but as containing different amounts of carbonaceous flaws, each with different flaw spacing, size and shape. The mechanical properties of interest in the Krell and Strassburger [36] work were hardness, Young's modulus, and the uniaxial compressive strength. The ballistic performance metric used in their paper was the depth of penetration (DoP), and the conclusion of Krell and Strassburger [36] was that fragmentation was the single most important mechanism for resisting penetration. Moynihan et al. [37] also establish the importance of fragmentation on the perforation resistance of boron carbide. We note that much of the fragmentation is confined in such tests.

Fragmentation, itself, is a low-energy process in that the percentage of input energy that is dissipated in the generation of fragments can be very low (<2% [38, 39]). Similar conversion rates have been reported during impact tests [40, 41]. The majority of the ballistic impact energy may be dissipated in processes that occur after the onset of fragmentation. Studies have shown that > 40 % of the impactor kinetic energy can be transferred to the debris during impact into brittle materials [42, 43].

The effects of fragmentation on penetration resistance may increase the abrasive efficiency and, thus, projectile erosion. The effectiveness of fragments to erode the projectile is a function of their size, number and shape. In turn, these fragment statistics are a function of (among other things) the backing, material properties (e.g., strength, hardness, fracture toughness), grain size and the spacing between critically activated defects (from this study). In what follows, we examine the consequences of the key results summarized by Krell and Strassburger [36] coupled with our current understanding of the effects of microstructure and confinement on the failure and fragmentation of advanced ceramics. In particular, we use the result that the micro-structure dependence of fragmentation (i.e., Regime I) increases for increasing strain-rate and for increased confinement. We then use this new insight to explore the results of Sano et al. [24], who investigated strength and Knoop hardness effects on the ballistic performance of pressureless sintered and hot-pressed boron carbide.

4.3.1. Fragmentation and Ballistic Performance

In impact experiments into sapphire tiles, Krell and Strassburger [36] noted that smaller fragments correlated with less projectile damage and larger fragment sizes correlated to increased projectile damage. Stated more explicitly: larger fragments (relatively speaking) correlated well with increased ballistic performance. The average fragment sizes measured by Krell and Strassburger [36] were 330 μm (weaker ballistic performance) and 430 μm (improved ballistic performance), although they did not measure the numerous smaller fragments that were recorded in our present study. Nevertheless, we will assume that the objective is to obtain a larger average fragment size through material design in order to increase the ballistic performance. The results from our study suggest that an increased fragment size (and therefore by implication an improved ballistic performance) can be accomplished by increasing the spacing between graphitic disks. We use this insight to explain recent ballistic tests published in Sano et al. [24].

In their study, Sano et al. [24] investigated the ballistic performance of two boron carbide materials: hot-pressed pressure-aided densified (PAD) and pressureless sintered material (PS). There was a noted inferiority of the PS material in its ballistic performance, including considerably more variability in its penetration resistance over a range of normalized impact velocities. Although the goal of their study was to link the ballistic performance of boron carbide tiles with uniaxial compressive strength and Knoop hardness measurements, this was not successful. The images in Sano et al. [24] show that the PS material has a significantly greater number of carbonaceous flaws in comparison to the PAD material. Using results from our present study, an increased graphite defect population would result in smaller fragments for the PS material than the PAD material and, thus, an inferior ballistic performance by PS. In this analysis, we do not consider boron carbide grain sizes and texture, which also play some role in the ballistic performance of the PS and PAD materials.

4.3.2. Microstructure, Mechanical Properties and Ballistic Performance

Lastly, we briefly discuss why strength may perhaps not be a strong indicator of ballistic performance, as Krell and Strassburger [36] indicated and Sano et al. [24] pointed out, despite this property likely being related to fragmentation (equations (9) and (10)). In impact experiments into different types of sapphire tiles, Krell and Strassburger [36] note a significant increase in ballistic performance when the average fragment size increases by 30 % (330 μm to 430 μm). Generally, we consider a domain for which the strain rate is sufficiently high enough that microstructure-dependent fragmentation dominates the fragmentation distributions. Let's also assume that the average fragment size ($\bar{\ell}$) and mean flaw spacing ($\bar{\ell}_n$) are equivalent. Thus, a 30 % increase in fragment size would require a 30 % increase in mean flaw spacing ($\bar{\ell}_n$), resulting in an associated decrease in flaw density (η: #/m^3) of 45 % (since $\bar{\ell}_n \approx \eta^{-1/3}$). Kimberley et al. [25] developed a scaling relationship linking compressive strength and flaw density (i.e., $\sigma_c \propto \eta^{-1/4}$), therefore a 45 % decrease in flaw density would result in a 22 % increase in strength. Based on available experimental measurements of uniaxial compressive strengths provided in studies by Sano et al. [24, 44], in-test variations can range between 8% and 16%. Thus, when the in-test variations are compounded (i.e., 16 % to 32 %), a 22 % difference in strength cannot show statstical significance. For these reasons, both positive and negative correlations of strength (e.g., bending vs compressive, dynamic vs. static) and ballistic performance can be concluded, and these have been noted by Krell and Strassburger [36]. All together, determining statistically significant differences in strengths between the two sapphire materials in the Krell and Strassburger [36] is not achievable with current testing approaches.

5. Concluding Remarks

Prediction of ceramic performance is central in developing the next generation of brittle armor materials. This may be made possible through the inclusion of realistic microstructures and failure mechanisms into numerical codes and with quantitative comparison with failure and fragmentation mechanisms under well-defined dynamic loading conditions. In this study, the effects of the microstructure on the uniaxial and bi-axial compressive failure and fragmentation of a hot-pressed boron carbide were investigated. We showed that there exists two compressive fragmentation mechanisms for these rates and stress states. One mechanism, associated with smaller fragments, is linked with the spacing between a critically activated defect type (in this case graphitic disks in boron carbide). The second fragmentation mechanism is associated with the failure of the structure rather than just the material.

6. Acknowledgments

This research was sponsored by the Army Research Laboratory and was accomplished under Cooperative Agreement Number W911NF-12-2-0022. The views and conclusions contained in this document are those of the authors and should not be interpreted as representing the official policies, either expressed or implied, of the Army Research Laboratory or the U.S. Government. The U.S. Government is authorized to reproduce and distribute reprints for Government purposes notwithstanding any copyright notation herein. Justin Wilkerson, Debjoy Mallick, Andy Tonge, and Nitin Daphalapurkar are thanked for many discussion on brittle fragmentation. Kanak Kuwelkar is acknowledged for discussions of the microstructure. Matt Bratcher is also acknowledged for the ulstrasound measurements, and Kevin Peters and Wesley Baire for taking many images of fragments. Lastly, Jeff Swab and Jerry LaSalvia are acknowledged for many insightful discussions on advanced ceramics.

7. References

[1] H. Wang, K. Ramesh, Dynamic strength and fragmentation of hot-pressed silicon carbide under uniaxial compression, Acta Materialia 52 (2) (2004) 355 – 367.

[2] M. Bakas, J. W. McCauley, V. Greenhut, D. Niesz, R. Haber, B. West, Quantitative analysis of inclusion distributions in hot pressed silicon carbide, International Journal of Impact Engineering.

[3] G. Hu, K. Ramesh, B. Cao, J. McCauley, The compressive failure of aluminum nitride considered as a model advanced ceramic, Journal of the Mechanics and Physics of Solids 59 (5) (2011) 1076 – 1093.

[4] J. LaSalvia, Recent progress on the influence of microstructure and mechanical properties on ballistic performance, Ceramic transactions 134 (2002) 557–570.

[5] M. Chen, J. W. McCauley, K. J. Hemker, Shock-induced localized amorphization in boron carbide, Science 299 (5612) (2003) 1563–1566.

[6] B. Paliwal, K. T. Ramesh, J. W. McCauley, M. Chen, Dynamic compressive failure of alon under controlled planar confinement, Journal of the American Ceramic Society 91 (11) (2008) 3619–3629.

[7] L. Graham-Brady, Statistical characterization of meso-scale uniaxial compressive strength in brittle materials with randomly occurring flaws, International Journal of Solids and Structures 47 (1819).

[8] J. Kimberley, K. Ramesh, N. Daphalapurkar, A scaling law for the dynamic strength of brittle solids, Acta Materialia 61 (9) (2013) 3509 – 3521.

[9] M. L. Wilkins, Mechanics of penetration and perforation, International Journal of Engineering Science 16 (11) (1978) 793 – 807, special Issue: Penetration Mechanics.

[10] J. J. Swab, A. A. Wereszczak, J. Pritchett, K. Johanns, Influence of microstructure on the indentation-induced damage in silicon carbide, Advances in Ceramic Armor II: Ceramic Engineering and Science Proceedings, Volume 27, Issue 7 (2007) 251–259.

[11] C. E. Anderson, B. L. Morris, The ballistic performance of confined al_2o_3 ceramic tiles, International Journal of Impact Engineering 12 (2) (1992) 167 – 187.

[12] W. W. Chen, A. Rajendran, B. Song, X. Nie, Dynamic fracture of ceramics in armor applications, Journal of the American Ceramic Society 90 (4) (2007) 1005–1018.

[13] D. Stepp, Damage mitigation in ceramics: Historical developments and future directions in army research, Ceramic transactions 134 (2002) 421–428.

[14] N. Mott, A theory of the fragmentation of shells and bombs, Technical Report AC4035, United Kingdom Ministry of Supply (May 1943).

[15] N. Mott, Fragmentation of shell cases, Technical Report A189: 300308, Proceedings of the Royal Society (1947).

[16] D. E. Grady, Fragmentation of rings and shells: the legacy of N.F. Mott, Springer, 2006.

[17] D. E. Grady, Local inertial effects in dynamic fragmentation, Journal of Applied Physics 53 (1) (1982) 322–325.

[18] J. D. Hogan, J. A. Castillo, A. Rawle, J. G. Spray, R. J. Rogers, Automated microscopy and particle size analysis of dynamic fragmentation in natural ceramics, Engineering Fracture Mechanics 98 (0) (2013) 80 – 91.

[19] L. A. Glenn, A. Chudnovsky, Strain and energy effects on dynamic fragmentation, Journal of Applied Physics 59 (4) (1986) 1379 –1380.

[20] F. Zhou, J. F. Molinari, K. Ramesh, Analysis of the brittle fragmentation of an expanding ring, Computational Materials Science 37 (1-2) (2006) 74 – 85.

[21] F. Zhou, J. F. Molinari, K. T. Ramesh, Effects of material properties on the fragmentation of brittle materials, International Journal of Fracture 139 (2006) 169–196.

[22] S. Levy, J. Molinari, Dynamic fragmentation of ceramics, signature of defects and scaling of fragment sizes, Journal of the Mechanics and Physics of Solids 58 (1) (2010) 12 – 26.

[23] J. D. Hogan, R. J. Rogers, J. G. Spray, S. Boonsue, Dynamic fragmentation of granite for impact energies of 6 to 28 j, Engineering Fracture Mechanics 79 (0) (2012) 103 – 125.

[24] T. Sano, M. Shaeffer, L. Vargas-Gonzalez, J. Pomerantz, High strain rate performance of pressureless sintered boron carbide, in: Dynamic Behavior of Materials, Volume 1, Springer, 2014, pp. 13–19.

[25] J. Kimberley, K. Ramesh, N. Daphalapurkar, A scaling law for the dynamic strength of brittle solids, Acta Materialia 61 (9) (2013) 3509–3521.

[26] S. Nemat-Nasser, H. Horii, Compression-induced nonplanar crack extension with application to splitting, exfoliation, and rockburst, Journal of Geophysical Research 87 (B8) (1982) 6805–6821.

[27] M. Ashby, S. H. N. Cooksley), The failure of brittle solids containing small cracks under compressive stress states, Acta Metallurgica 34 (3) (1986) 497 – 510.

[28] G. Ravichandran, G. Subhash, A micromechanical model for high strain rate behavior of ceramics, International Journal of Solids and Structures 32 (1718) (1995) 2627 – 2646.

[29] B. Paliwal, K. Ramesh, An interacting micro-crack damage model for failure of brittle materials under compression, Journal of the Mechanics and Physics of Solids 56 (3) (2008) 896–923.

[30] E. Bombolakis, Study of the brittle fracture process under uniaxial compression, Tectonophysics 18 (34) (1973) 231 – 248.

[31] H. Horii, S. Nemat-Nasser, Compression-induced microcrack growth in brittle solids: Axial splitting and shear failure, Journal of Geophysical Research: Solid Earth (1978–2012) 90 (B4) (1985) 3105–3125.

[32] D. E. Grady, Length scales and size distributions in dynamic fragmentation, International Journal of Fracture 163 (1–2) (2009) 85–99.

[33] W. Drugan, Dynamic fragmentation of brittle materials: analytical mechanics-based models, Journal of the Mechanics and Physics of Solids 49 (6) (2001) 1181 – 1208. doi:10.1016/S0022-5096(01)00002-3.

[34] V. Shenoy, K.-S. Kim, Disorder effects in dynamic fragmentation of brittle materials, Journal of the Mechanics and Physics of Solids 51 (1112) (2003) 2023 – 2035.

[35] A. Charles, Handbook of ceramics, glasses, and diamonds (2001).

[36] A. Krell, E. Strassburger, Order of influences on the ballistic resistance of armor ceramics and single crystals, Materials Science and Engineering: A 597 (0) (2014) 422 – 430.

[37] T. Moynihan, J. LaSalvia, M. Burkins, Analysis of shatter gap phenomenon in a

boron carbide/composite laminate armor system, in: Proceedings of International Ballistics Symposium Sept, 2002.

[38] D. Tromans, Mineral comminution: Energy efficiency considerations, Minerals Engineering 21 (8) (2008) 613 – 620.

[39] D. Tromans, J. Meech, Fracture toughness and surface energies of minerals: theoretical estimates for oxides, sulphides, silicates and halides, Minerals Engineering 15 (12) (2002) 1027 – 1041.

[40] R. Woodward, W. Gooch, Jr, R. O'Donnell, W. Perciballi, B. Baxter, S. Pattie, A study of fragmentation in the ballistic impact of ceramics, International Journal of Impact Engineering 15 (5) (1994) 605 – 618.

[41] J. D. Hogan, J. G. Spray, R. J. Rogers, S. Boonsue, G. Vincent, M. Schneider, Micro-scale energy dissipation mechanisms during dynamic fracture in natural polyphase ceramic blocks, International Journal of Impact Engineering 38 (12) (2011) 931 – 939.

[42] R. L. Woodward, A simple one-dimensional approach to modelling ceramic composite armour defeat, International Journal of Impact Engineering 9 (4) (1990) 455–474.

[43] J. D. Hogan, J. G. Spray, R. J. Rogers, G. Vincent, M. Schneider, Dynamic fragmentation of planetary materials: ejecta length quantification and semi-analytical modelling, International Journal of Impact Engineering 62 (2013) 219–228.

[44] T. Sano, E. Chin, B. Paliwal, M. Chen, Comparison of slip cast and hot pressed

boron carbide, Processing and properties of advanced ceramics and composites: ceramic transactions 203.

List of Tables

1 Material properties for boron carbide used in the theoretical prediction of average fragment size. 37

2 Calculation of the characteristic size and strain rate 37

3 Summary of average Regime II fragment size ($\bar{\ell}$) and deviotoric stress (σ') and estimated equivalent strain rates ($\dot{\epsilon}_{equi}$). QS: quasi-static, Dyn: dynamic, UC: uniaxial compression, BiC: bi-axial confined compression. The bi-axial confined cases are for a confining pressure of 500 MPa. 37

List of Figures

1 Schematic of Kolsky bar arrangement with inset of the boron carbide sample and bi-axial confinement apparatus. 38

2 Optical microscope images of the boron carbide microstructure illustrating: (a) the various types of microstructure defects and inclusions, and (b) converted monochrome image used to determine the spacing between graphite disks. 38

3 Schematic of image processing technique used to characterize and classify the microstructure features. 39

4 Stress-time history of dynamic uniaxial compression of boron carbide with time-resolved high-speed video images showing mesoscale failure mechanisms. The dashed line is the linear fit of 10 and 90 % of the peak stress and this corresponds to the stress rate $\dot{\sigma}$=200 MPa/μs. 39

5 Stress-time history of bi-axial compression of boron carbide with time-resolved high-speed video images showing mesoscale failure mechanisms. The confining pressure is 300 MPa. The dashed line is the linear fit of 10 and 90 % of the peak stress and this corresponds to the stress rate $\dot{\sigma}$=175/MPa μs. 40

6 Cumulative distributions of major axis fragment size (ℓ: μm) and fragment spacing (ℓ_n) for quasi-static and dynamic uniaxial and biaxial compression (confining pressure 500 MPa). The thin blue lines are for the uniaxial compressive case, and the thick red lines are for the confined compression case. Dashed lines correspond to the higher rate experiments. The solid green curve on the extreme left is the distribution of graphite disk spacing. 41

7 Optical microscope image of internal features of a boron carbide fragment (take for the dynamic uniaxial compression tests) showing graphite disks intersecting the fracture surface. 42

8 Quantile-quantile plot comparing graphitic disk spacing and Regime I fragment sizes for the dynamic bi-axial compression case (confining pressure 500 MPa). The overlapping of the two curves suggests the distributions are similar up to 70 μm. 42

9 Plot of circularity ($2(\pi A)^{0.5}/P$) against major axis size for: (a) dynamic uniaxial compression and (b) dynamic bi-axially confined compression (confining pressure 500 MPa). Different fragmentation regions are hypothesized. 43

10 Comparison of theoretical prediction of fragment sizes with experimental results. The fragment size is normalized by the characteristic size (L_0) and the strain rate is normalized by the characteristic strain rate ($\dot{\epsilon}_0$) proposed by Zhou et al. [21]. 43

Table 1: Material properties for boron carbide used in the theoretical prediction of average fragment size.

Material	ρ (kg/m^3)	E (GPa)	c ($\sqrt{E/\rho}$: km/s)	K_{Ic} (MPa $\sqrt{m}$)	G_c (N/m)	σ_t (σ_c/10: GPa)
Boron Carbide	2,490	430	12.7	2.5	7.70	0.285

Table 2: Calculation of the characteristic size and strain rate

Material	L_0 (μm)	$\dot{\epsilon}_0$ (s^{-1})
Boron Carbide	38.5	2.33x10^5

Table 3: Summary of average Regime II fragment size ($\bar{\ell}$) and deviotoric stress (σ') and estimated equivalent strain rates ($\dot{\epsilon}_{equi}$). QS: quasi-static, Dyn: dynamic, UC: uniaxial compression, BiC: bi-axial confined compression. The bi-axial confined cases are for a confining pressure of 500 MPa.

Test Case	$\bar{\ell}$ (μm)	σ' (Pa)	$\dot{\epsilon}_{equi}$ (s^{-1})
QS UC	355±217	2.55	67
QS UC	322±207	2.85	60
Dyn UC	278±203	4.10	86
Dyn UC	316±228	3.62	97
QS BiC	335±218	3.03	72
QS BiC	320±194	3.40	81
Dyn BiC	259±211	4.10	97
Dyn BiC	247±191	3.90	92

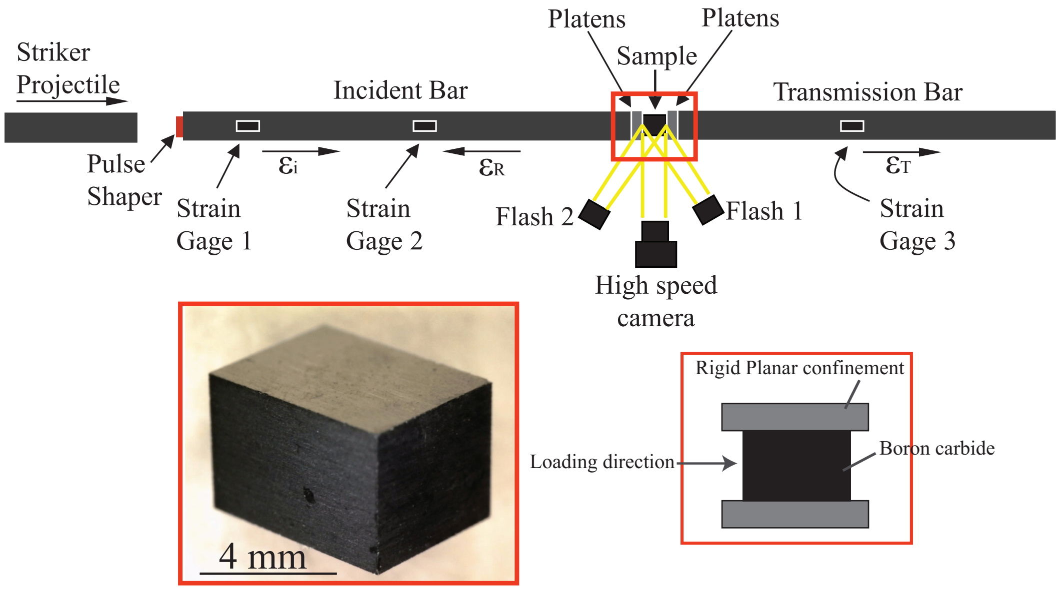

Fig. 1: Schematic of Kolsky bar arrangement with inset of the boron carbide sample and bi-axial confinement apparatus.

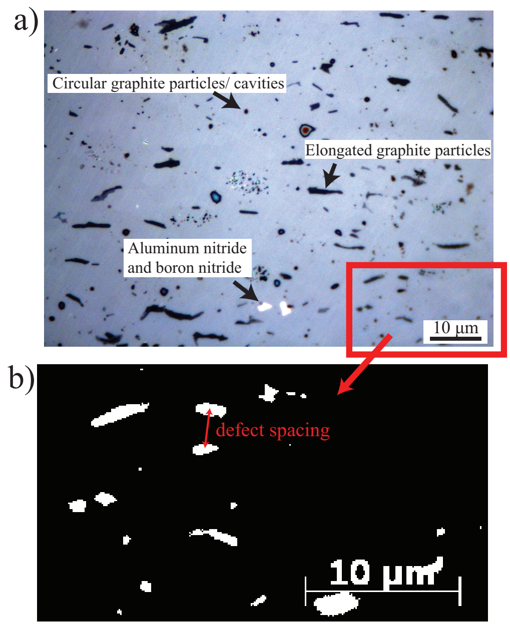

Fig. 2: Optical microscope images of the boron carbide microstructure illustrating: (a) the various types of microstructure defects and inclusions, and (b) converted monochrome image used to determine the spacing between graphite disks.

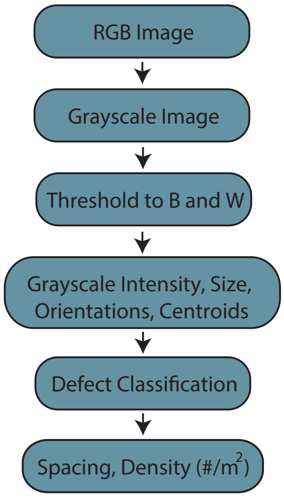

Fig. 3: Schematic of image processing technique used to characterize and classify the microstructure features.

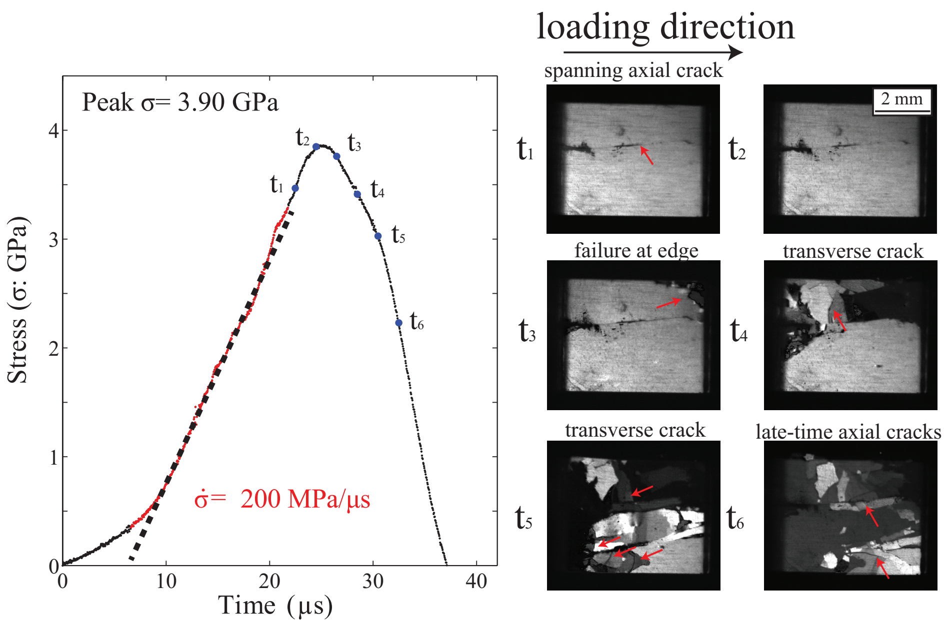

Fig. 4: Stress-time history of dynamic uniaxial compression of boron carbide with time-resolved high-speed video images showing mesoscale failure mechanisms. The dashed line is the linear fit of 10 and 90 % of the peak stress and this corresponds to the stress rate $\dot{\sigma}$=200 MPa/μs.

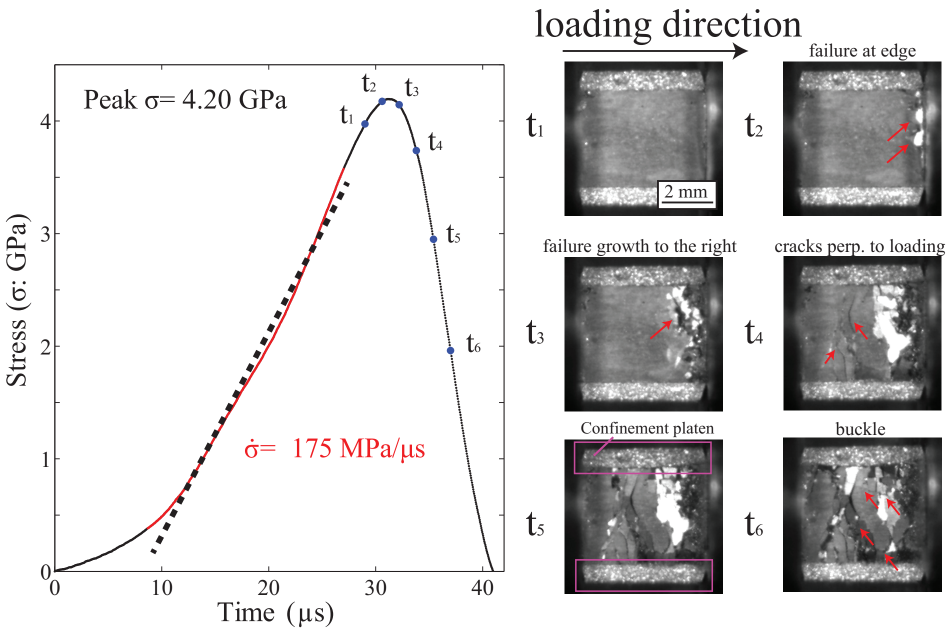

Fig. 5: Stress-time history of bi-axial compression of boron carbide with time-resolved high-speed video images showing mesoscale failure mechanisms. The confining pressure is 300 MPa. The dashed line is the linear fit of 10 and 90 % of the peak stress and this corresponds to the stress rate $\dot{\sigma}$=175/MPa μs.

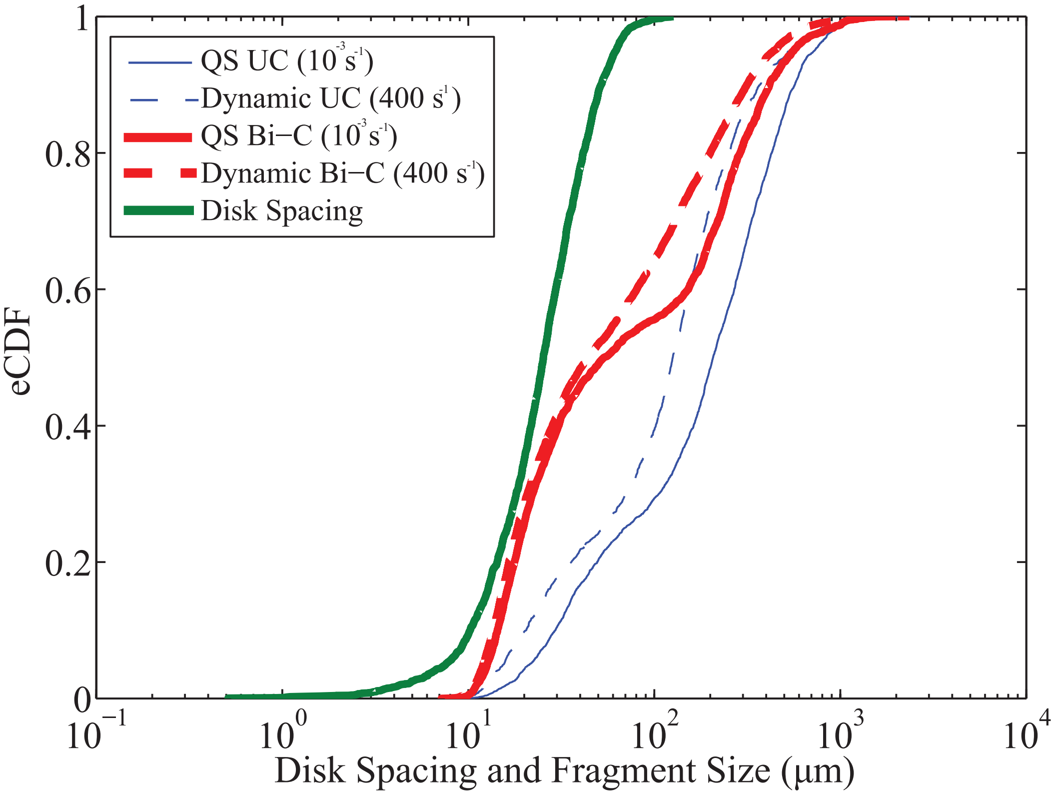

Fig. 6: Cumulative distributions of major axis fragment size (ℓ: μm) and fragment spacing (ℓ_n) for quasi-static and dynamic uniaxial and biaxial compression (confining pressure 500 MPa). The thin blue lines are for the uniaxial compressive case, and the thick red lines are for the confined compression case. Dashed lines correspond to the higher rate experiments. The solid green curve on the extreme left is the distribution of graphite disk spacing.

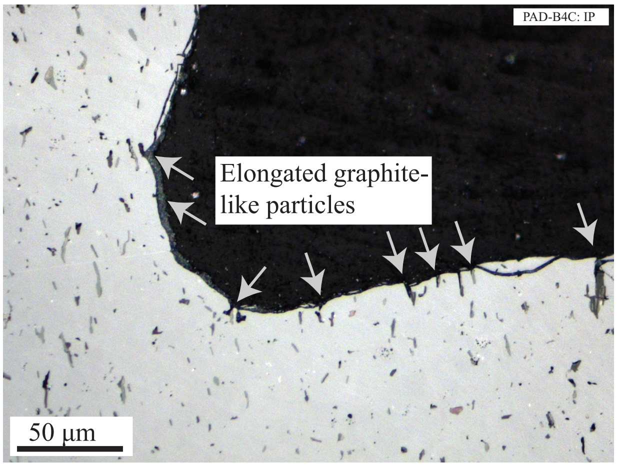

Fig. 7: Optical microscope image of internal features of a boron carbide fragment (take for the dynamic uniaxial compression tests) showing graphite disks intersecting the fracture surface.

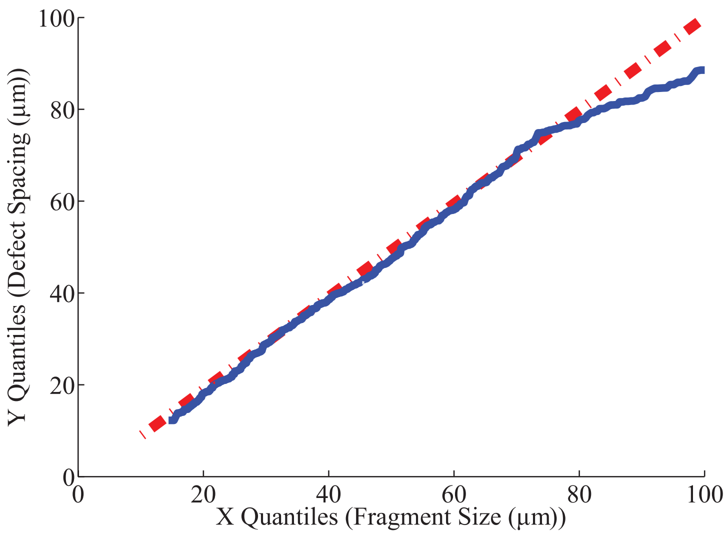

Fig. 8: Quantile-quantile plot comparing graphitic disk spacing and Regime I fragment sizes for the dynamic bi-axial compression case (confining pressure 500 MPa). The overlapping of the two curves suggests the distributions are similar up to 70 μm.

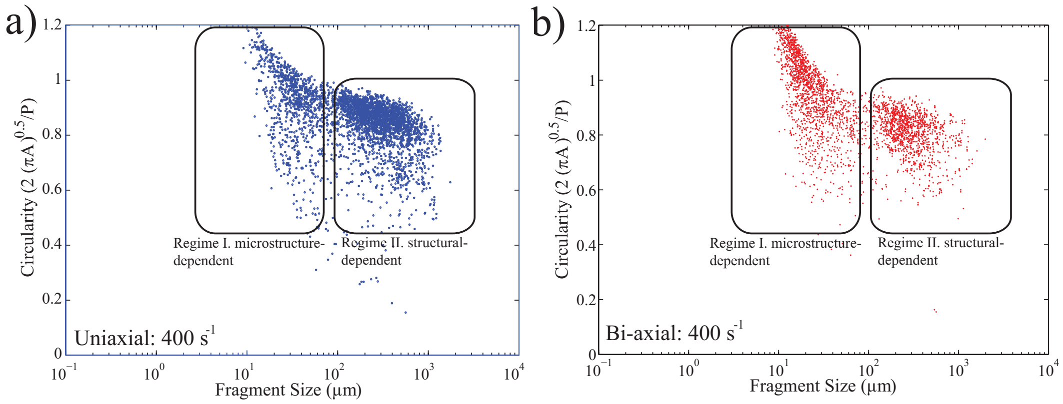

Fig. 9: Plot of circularity ($2(\pi A)^{0.5}/P$) against major axis size for: (a) dynamic uniaxial compression and (b) dynamic bi-axially confined compression (confining pressure 500 MPa). Different fragmentation regions are hypothesized.

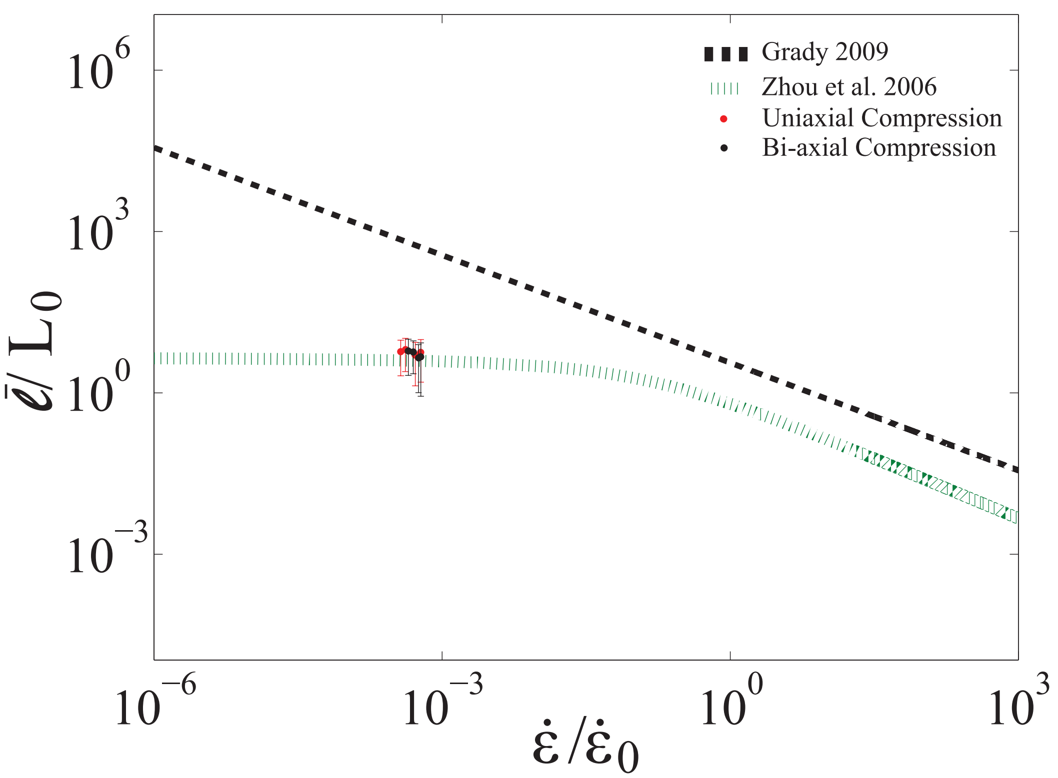

Fig. 10: Comparison of theoretical prediction of fragment sizes with experimental results. The fragment size is normalized by the characteristic size (L_0) and the strain rate is normalized by the characteristic strain rate ($\dot{\epsilon}_0$) proposed by Zhou et al. [21].